

Dissolution Processes at Step Edges of Calcite in Water Investigated by High-Speed Frequency Modulation Atomic Force Microscopy and Simulation

メタデータ	言語: eng 出版者: 公開日: 2017-12-05 キーワード (Ja): キーワード (En): 作成者: メールアドレス: 所属:
URL	https://doi.org/10.24517/00010850

This work is licensed under a Creative Commons Attribution-NonCommercial-ShareAlike 3.0 International License.



Dissolution Processes at Step Edges of Calcite in Water Investigated by High-Speed Frequency Modulation Atomic Force Microscopy and Simulation

Kazuki Miyata,^{†,||} John Tracey,[‡] Keisuke Miyazawa,[†] Ville Haapasilta,[‡] Peter Spijker,[‡] Yuta Kawagoe,[†] Adam S. Foster,^{,†,‡} Katsuo Tsukamoto,[§] Takeshi Fukuma^{*,†,⊥}*

[†] Division of Electrical Engineering and Computer Science, Kanazawa University, Kanazawa 920-1192, Japan

[‡] COMP Centre of Excellence, Department of Applied Physics, Aalto University, Helsinki FI-00076, Finland

[§] Department of Earth and Planetary Materials Science Graduate School of Science, Tohoku University, Aramaki, Aoba, Sendai 980-8578, Japan

[⊥] ACT-C, Japan Science and Technology Agency, Saitama 332-0012, Japan

ABSTRACT:

The microscopic understanding of the crystal growth and dissolution processes have been greatly advanced by the direct imaging of nanoscale step flows by atomic force microscopy (AFM), optical interferometry and x-ray microscopy. However, one of the most fundamental events that govern their kinetics, namely, atomistic events at the step edges have not been well understood. In this study, we have developed high-speed frequency modulation AFM (FM-AFM) and enabled true atomic-resolution imaging in liquid at ~ 1 s/frame, which is ~ 50 times faster than the conventional FM-AFM. With the developed AFM, we have directly imaged subnanometer-scale surface structures around the moving step edges of calcite during its dissolution in water. The obtained images reveal that the transition region with typical width of a few nanometers is formed along the step edges. Building upon insight in previous studies, our simulations suggest that the transition region is most likely to be a $\text{Ca}(\text{OH})_2$ monolayer formed as an intermediate state in the dissolution process. Based on this finding, we improve our understanding of the atomistic dissolution model of calcite in water. These results open up a wide range of future applications of the high-speed FM-AFM to the studies on various dynamic processes at solid-liquid interfaces with true atomic resolution.

KEYWORDS: Atomic force microscopy, high-speed atomic-resolution imaging, crystal dissolution process, calcite

MAIN TEXT:

Calcite (CaCO_3) constitutes the largest carbon reservoir on Earth¹ and its dissolution plays a major role in the global carbon cycle in nature^{2, 3}, as well as in technologies such as geologic CO_2

sequestration (GCS)⁴. In previous studies, several dissolution models⁵⁻⁹ have been proposed to explain the experimental results obtained by the macroscopic elemental analyses^{5, 6} and nanoscale step flow measurements^{7,8,10-12}. Based on these models and semi-empirically determined parameters, Monte Carlo simulations successfully predicted dissolution processes under various conditions^{9,12,13}.

In the meanwhile, efforts have been made for understanding atomistic processes at the step edges. Shiraki *et al.* investigated pH and CO₂ pressure dependence of the step flow rate by AFM and presented a detailed atomistic model of the chemical reaction at the step edges⁵. In this model, the reaction is triggered by the dissociative adsorption of a water molecule and leads to the desorption of an ion pair [HCO₃·Ca]⁺. Although they did not present direct atomic-scale evidence to support this model, the possibility of the dissociative adsorption of water was previously suggested by other studies using infrared (IR) spectroscopy^{14,15} or x-ray photoelectron spectroscopy (XPS)¹⁶. Kerisit *et al.* performed atomistic simulations of water-calcite interaction and calculated the energetics for the removal of carbonate groups in water¹⁷. They suggested that the dissociative adsorption of water is unlikely on a flat terrace, but possible at the step edges. They also tentatively suggested the possibility of a two-step dissolution pathway, where CO₃²⁻ and Ca²⁺ are not removed simultaneously, but separately. Lardge *et al.* performed *ab initio* simulations of water adsorption near step edges and vacancies¹⁸, revealing that associative adsorption is favored except on carbonate vacancies, where water molecules dissociate to form bicarbonate and hydroxide ions.

While these previous studies consistently implied the critical contribution of the dissociative adsorption of water to the dissolution process, a detailed reaction pathway and corresponding model have not been established. This is largely due to the lack of a method able to visualize

subnanometer-scale surface structures around the moving step edges. Atomic force microscopy (AFM) is one of the most promising tools to solve this problem. However, conventional AFM techniques do not have sufficient temporal or spatial resolution. Ando *et al.* developed high-speed amplitude modulation AFM that enabled direct visualization of protein dynamics¹⁹, but its spatial resolution has been limited to ~ 1 nm. Fukuma *et al.* developed liquid-environment frequency modulation AFM (FM-AFM) and enabled true atomic-resolution imaging in liquid²⁰, but its imaging speed has been limited to ~ 1 min/frame. Till date, there is no method for visualizing atomic-scale dynamic processes at a solid-liquid interface.

In this study, we have developed high-speed FM-AFM (Figure 1a) and enabled true atomic-resolution imaging in liquid at ~ 1 s/frame, which is ~ 50 times faster than the conventional FM-

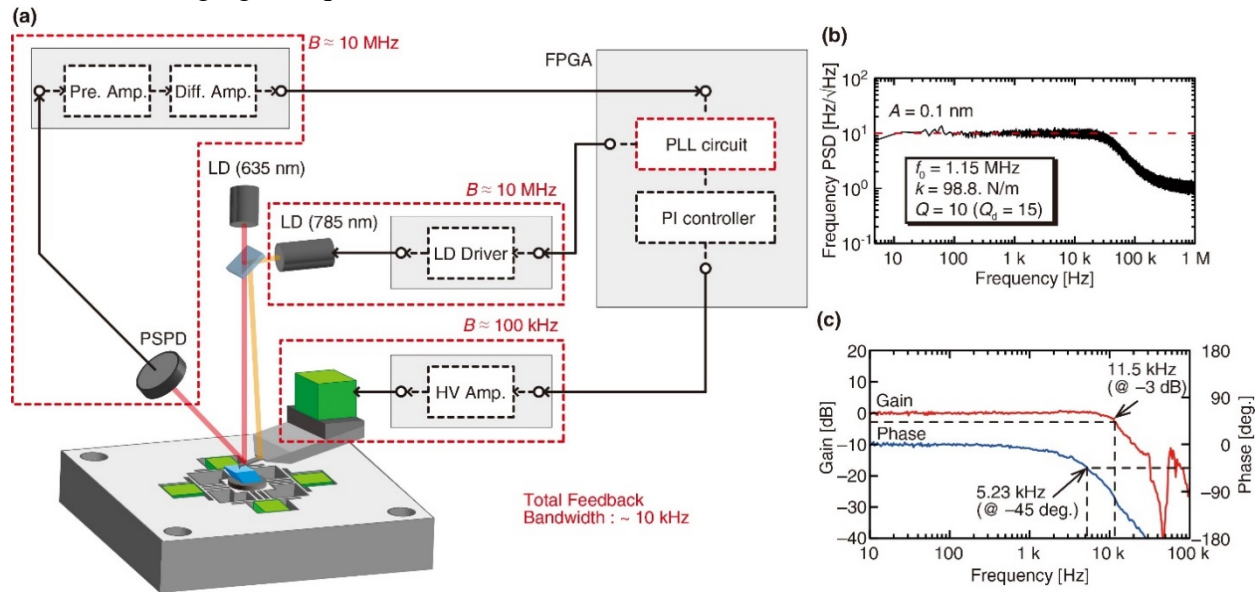


Figure 1. Setup and performance of the developed high-speed FM-AFM. (a) Setup. (b) Power spectral density (PSD) distribution of the frequency shift signal. The solid line indicates the raw data while the dotted line indicates the thermal-noise-limited performance. Q and Q_d denote the Q factors measured with and without driving the cantilever, respectively. (c) Frequency response of the tip-sample distance regulation. These measurements were performed with a small cantilever (AC55, Olympus) in water. The roll off frequency (~ 56 kHz) observed in (b) corresponds to the bandwidth of the PLL and strongly depends on f_0 . For an ultra-short cantilever (USC, Nanoworld), it becomes ~ 165 kHz owing to its high f_0 (~ 3.5 MHz in liquid).

AFM. With the developed system, we directly image subnanometer-scale surface structures around the moving step edges of calcite during its dissolution in water. Based on the obtained images and our simulation results, we improve our understanding on the atomistic calcite dissolution model.

To improve the operation speed of FM-AFM without losing its capability of true atomic-resolution imaging, we should satisfy two major requirements. One of them is a sufficient force resolution. True atomic-resolution imaging by FM-AFM typically requires ~ 10 pN force resolution. To satisfy this requirement with a standard cantilever in liquid, the measurement bandwidth (B) is limited to ~ 100 Hz. To enhance B , we used a small cantilever with a megahertz-order resonance frequency (f_0) in liquid²¹. Owing to the high f_0 , it can provide a ~ 10 pN force resolution even with a ~ 5 kHz bandwidth. Note that this performance is available only when the noise from the instruments is smaller than that from the thermal vibration of the cantilever. To meet this requirement, we developed a wideband, low noise and highly stable cantilever deflection sensor^{22–24}, photothermal cantilever excitation system^{21, 24} and digital phase-locked loop (PLL) circuit^{25, 26}. With these improvements, we achieved thermal-noise-limited performance even with a small cantilever, as shown in Figure 1b. This figure shows that the experimentally measured noise density of the frequency shift signal (solid line) agrees with the thermal-noise-limited performance (dotted line).

Another requirement is a sufficient bandwidth of the tip-sample distance regulation. To achieve this goal, we improved every component constituting the feedback loop. This includes the components described above, the separate-type XY-sample and Z-tip scanners^{27, 28} and the high-voltage amplifier²⁷. The PLL circuit and the other basic AFM control functions such as the proportional-integral controller, the scan controller and the data acquisition system were all implemented in a single field programmable gate array (FPGA) chip to minimize the latency²⁶. With these improvements, we achieved the total feedback bandwidth of ~ 10 kHz at -3 dB gain and

~5 kHz at -45 deg. phase as shown in Figure 1c. This is approximately 50 times faster than the conventional FM-AFM, enabling true atomic-resolution imaging at ~ 1 sec/frame in liquid.

The cleaved $(10\bar{1}4)$ calcite surface consists of Ca and CO_3 ions (Figure 2a). In pure water, rhombic pits are created on a flat terrace, and their step edges propagate during dissolution. Using our high-speed FM-AFM, we imaged one of the propagating step edges at 2 s/frame. Figure 2b shows three snapshots from among the successive images in Supplementary Video 1. The step edge propagates from the lower right to the upper left corner at ~ 0.4 nm/s. Owing to the fast imaging speed, displacement of the step during the one-frame scan was ~ 0.8 nm. Thus, the image distortion is

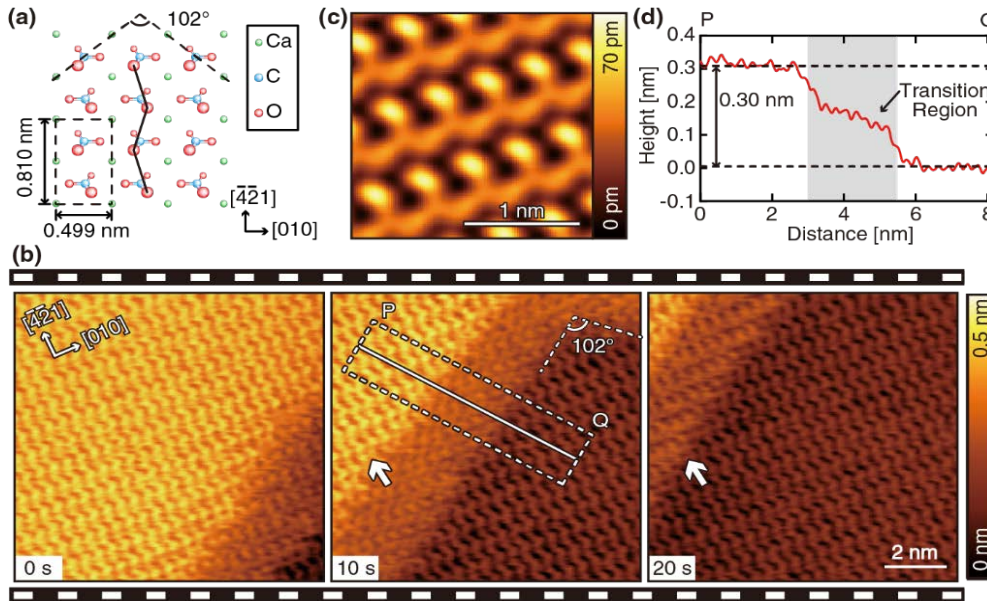


Figure 2. High-speed FM-AFM images of calcite dissolution in water. (a) Atomistic model of the calcite $(10\bar{1}4)$ surface. (b) Snapshots of the successive FM-AFM images of the calcite surface in water. 2 s/frame. 500×500 pix². (c) Correlation averaged image of the transition region. (d) Averaged height profile measured along line PQ indicated in (b). The dotted lines around line PQ indicate the width of the averaging.

almost negligible. In fact, the observed angle between the two adjacent steps ($\sim 102^\circ$) corresponds to the value expected from the crystallographic surface structure (Figure 2a).

The obtained images reveal an intermediate transition region with a dotted-line contrast, in addition to the upper and lower terraces with the zigzag-line contrast. This contrast pattern is more clearly seen in the correlation averaged image (Figure 2c). The cross-sectional profile measured across the step edge (Figure 2d) shows that the height difference between the two terraces is 0.30 nm, consistent with the single step height of the calcite (10 $\bar{1}$ 4) surface. Meanwhile, the transition region shows an intermediate height of 0.12–0.18 nm from the lower terrace.

In AFM observations, such an irregular structure at a step edge is often attributed to tip scan artifacts. However, we have strong evidence to exclude this possibility. The width of the transition region is not necessarily uniform and can change dynamically (Figure S1). The forward and backward scan images consistently show similar contrasts in the transition region (Figure S2). The transition region is reproducibly imaged with different tips and different samples (Figure S3), and hence cannot be explained by the double tip effect or feedback error, but represents a real feature of the solid-liquid interface structure.

The step flow rate of calcite has a relatively wide variation. In our experiments, it ranged from 0.08 nm/s to 1.20 nm/s (average: 0.36 nm/s, standard deviation: 0.29 nm/s for $n = 21$). Thus, even for a low speed imaging (~ 1 min/frame), we can take a few atomic-scale images while one step passes through the imaging area. Under such imaging conditions, the step edge is imaged as a slope rather than a step, and the transition region cannot be clearly recognized (see Figure S4 and its caption for detailed explanations on the imaging mechanism). This explains the lack of reports

on the transition region despite the considerable number of atomic-scale AFM images reported thus far^{29–31}.

To understand the physical origin of the transition region, we first investigated possible models that do not involve dissociative adsorption of water. One is an irregular hydration structure formed at the step edges. However, the water density map obtained by our molecular dynamics (MD) simulation reveals that the influence of the step edge decays within ~0.5 nm (Figure S5), consistent with past studies^{32, 33}. The estimated width of the irregular hydration structure is too small to explain the transition region that has a width of 2–25 nm (Figure S1). Another possible model is transient relaxation before or after the dissolution. However, the FM-AFM images show that the lifetime of the transition region at a certain spot is ~10 s (arrows in Figure 2b), which is too long to be explained by atomistic surface relaxation. We also investigated the possibility of adsorption of the dissolved ions at the step edges by MD simulation, using adsorbed layers of Ca or CO₃ ions with or without counter ions in the hydrated or partially dehydrated state as the models (Figure S6). In all the cases, the adsorbed ions either desorbed or crystallized in < 1 ns. These results strongly suggest that the dissolution models that do not involve water dissociation cannot explain the presence of the transition region.

This conclusion is consistent with the previous studies, where the existence of the surface-bound OH groups was confirmed by IR and XPS analyses^{14–16} and the possibility of the water dissociation near the step edges was suggested by simulations^{17, 18}. If we assume the existence of water dissociation, the possible chemical reactions occurring at the step edges should be as below:





While reaction (1) describes the first step, reactions (2) and (3) show the two different pathways in the second step.

As per the general understanding of the stability of carbonic acid in bulk solution, reaction (2) should be dominant at neutral pH³⁴. To confirm this expectation, we performed the following density functional theory (DFT) calculations. We slightly (< 0.15 nm) displaced a CO_3^{2-} from the step edge in the presence of two water molecules and performed an energy optimization (Figure S7a). This displacement led to the dissociation of one water molecule to form HCO_3^- and CaOH^+ , while the other water molecule remained intact. The calculated formation energies of the four possible systems after water dissociation were less than -3.0 eV with respect to the intact step edge and two isolated water molecules (Figure S7b). In all the cases, the residual water did not dissociate during the energy optimization. These results confirm the first step described by reaction (1) and suggest that the second step described by reaction (3) is unfavorable. Furthermore, the formation energies of the systems after reactions (1)–(3) (Figure S8) indicated that the system after reaction (2) is -2 eV more favorable than the other two systems. In addition, the system after reaction (3) was unstable and returned to the original configuration during the energy optimization. These results consistently suggest that reaction (2) is more likely to occur in the second step.

The pathway described by reactions (1) and (2) suggests two possible models of the transition region: an adsorbed layer of CaOH^+ with HCO_3^- (Model I) and $\text{Ca}(\text{OH})_2$ (Model II). We prepared setups for both possible transition region models (Figure S9a and 3a), including a full solid-liquid interface and performed classical MD simulations for 7.5 ns to understand the distribution and stability of the water and ions near the step edges. In contrast to the case of the models without water dissociation (Figure S6), the ions were stably adsorbed on the surface during the whole simulation time for both the aforementioned models, further supporting the role of water dissociation in calcite dissolution. Comparison of the two simulation trajectories (Supplementary Videos 2 and 3) revealed a clear difference in the stability of the ions at surface. In Model I, the Ca^{2+} and OH^- ions were stably adsorbed on the calcite surface, but the HCO_3^- ions were loosely bound on the CaOH^+ layer and exhibit significant fluctuations in their positions. In contrast, the Ca^{2+} and OH^- ions in Model II were more stably adsorbed on the calcite surface. In experiments, if there are mobile species diffusing on the surface, we often see spike noises in the obtained

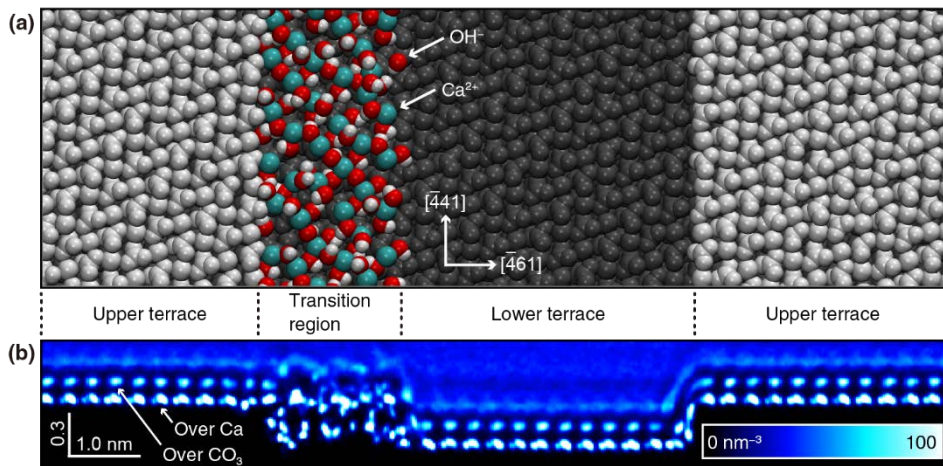


Figure 3. MD simulation of the calcite ($10\bar{1}4$) surface in water with a $\text{Ca}(\text{OH})_2$ layer at the step edge. (a) Snapshot of the simulation model at ~ 7.5 ns from the start. (b) $[441]$ projection of the water density map.

images. However, we did not see such indication of mobile species during the imaging of the transition region. Thus, Model II is more consistent with the experimental results and the observed transition region is more likely to be the $\text{Ca}(\text{OH})_2$ layer.

Since $\text{Ca}(\text{OH})_2$ is unstable in a bulk neutral solution³⁵, there must be a specific mechanism to stabilize the $\text{Ca}(\text{OH})_2$ layer at the step edges. Because of the relatively wide transition region, direct interaction between the step edge and the adsorbed ions cannot be the only mechanism underlying this stabilization. One possible explanation is the indirect interaction through the extended hydration structure. The hydration layers on the upper terrace can extend to the space over the transition region via the formation of a $\text{Ca}(\text{OH})_2$ layer (Figure 3b). The energetic merit to

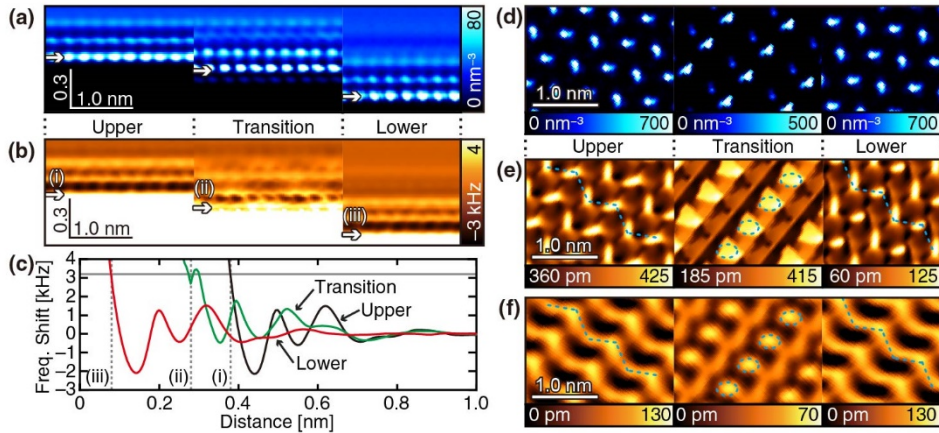


Figure 4. Comparison between the FM-AFM images of the transition region obtained by simulation and experiment. (a) $[\bar{4}41]$ projection of the water density map obtained by averaging the simulated distribution over each unit cell area. (b) $[\bar{4}41]$ projection of the Δf map calculated from (a). (c) Δf curves averaged over each region calculated from (b). (d) XY cross sections of (a) at the Z positions indicated by the arrows. (e) Height images obtained by simulating constant Δf mode imaging with a setpoint of 3.2 kHz. (f) Experimentally obtained FM-AFM images after the correlation averaging over each region.

form this extra hydrogen bonding network may allow the formation of a relatively wide adsorption layer.

To further confirm the validity of the proposed model, we compared the results obtained by the simulation and experiments (Figure 4). Here, since we are now interested in the details of the hydration structure on the transition region, rather than just its general stability with respect to dissolution, we performed further DFT calculations to establish the reliability of our model structure. Starting from initial models equivalent to those used in the beginning of the simulations in Figure 3, we found that DFT predicts a much more ordered structure for the transition region (see comparison in Figure S10). This structure was then used directly in the simulations of water structure across the whole system. The obtained water density map (Figure 4a) was averaged by a Gaussian filter, and converted to a force map and then to a Δf map (Figure 4b) using the solvent tip approximation (STA) model³⁶⁻³⁸ and Giessibl's approach³⁹. From the Δf map, the Z profiles averaged over each region were obtained (Figure 4c). Owing to the layer-like distribution of water, the Z profiles showed a clear oscillatory behavior. In FM-AFM, the vertical tip position is controlled such that the Δf is kept constant. We simulated this behavior by our virtual AFM (see Ref. [40] for details) and obtained FM-AFM images for various Δf setpoints. We compared them with the experimentally obtained images and found the best agreement at the setpoint of 3.2 kHz (gray solid line in Figure 4c). The average tip heights during the simulated imaging are indicated by the arrows (i)-(iii) in Figure 4b and the dotted lines (i)-(iii) in Figure 4c. These tip heights are consistent with the experimental fact that the transition region shows an intermediate height between the upper and lower terraces. The FM-AFM images (Figure 4e) obtained at these feedback positions show contrast patterns similar to those in the experimentally obtained images (Figure 4f). For example, a zigzag-line contrast at the upper and lower terraces, and a dotted-line contrast in

the transition region can be seen in both cases as indicated by the dotted lines. These characteristic features are also found in the XY cross sections (Figure 4d) of the water density map obtained at the Z positions (arrows in Figure 4a) corresponding to the average feedback positions (i)–(iii). This result reveals that these characteristic features reflect the water density distribution over each region. The 3.2 kHz setpoint assumed here is slightly higher than the value used for the actual FM-AFM experiment (2.86 kHz). However, the difference is within the error range expected from the STA model, where the AFM tip is approximated by a single water molecule. Overall, the simulation results agree well with the experimental results, further supporting the proposed model of the transition region.

Based on the finding of the transition region, here we propose an atomistic dissolution model (Figure 5). A water molecule on a calcite surface is strongly attracted to the Ca site with the oxygen

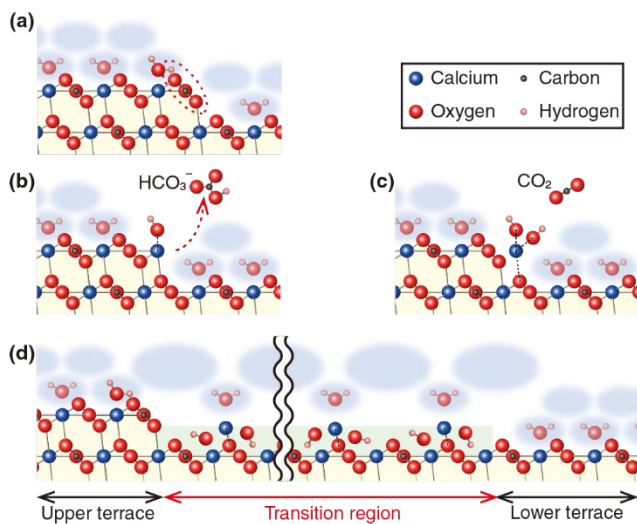


Figure 5. Atomistic dissolution model of calcite ($10\bar{1}4$) surface in water. (a) Proton transfer from the water to the carbonate ion. (b) Desorption of bicarbonate ion. (c) Transfer of a hydroxide ion from the bicarbonate ion to the surface Ca ion. (d) Formation of the transition region consisting of a $\text{Ca}(\text{OH})_2$ monolayer.

and hydrogen atoms oriented toward the Ca and CO₃ sites, respectively. Because of the strong attraction of the hydrogen atom to the CO₃ site, the proton is often transferred from the water molecule to the surface CO₃ ion. On a flat terrace, this proton is soon transferred back to reform the water molecule¹⁷. At a step edge, the proton transfer can lead to desorption of the HCO₃⁻ and the OH⁻ is left associated with the surface Ca ion. In the next step, the HCO₃⁻ is decomposed to produce a CO₂ and a second OH⁻ that adsorbs to the surface Ca and produces Ca(OH)₂. The energetic merit for forming an extended hydrogen bonding network from the upper terrace to the Ca(OH)₂ adsorption site stabilizes the adsorbed species on the surface. Repetition of these processes results in the formation of the observed Ca(OH)₂ layer, i.e. the transition region. The influence of the upper terrace on the hydration structure over the transition region should weaken as a function of the distance from the step edge and thus reduce the Ca(OH)₂ stability. This distance dependence determines the width of the transition region.

In the proposed model, we clarified the existence of an intermediate state (transition region) during calcite dissolution. This model supports the possibility of the sequential removal of CO₃²⁻ and Ca²⁺ ions from the step edge, which was previously suggested by Kerisit *et al.*¹⁷ based on their simulation results. The finding of the transition region has dramatically improved the real-space description of the hydration structure at the step edges (from Figure S5b to Figure 4a). Since the hydration exerts a vital influence on the adsorption of ions and organic molecules at the step edges⁴¹, the obtained knowledge should help us understand the atomic-scale origin of the major impact of such an adsorption on the dissolution kinetics^{42, 43}. The improved understanding on the atomistic dissolution model would, in turn, enable us to correlate the empirically determined kinetic parameters with the specific atomic-scale events. For example, the atomistic origin for the pH dependence of the calcite dissolution rate⁵ may be understood by taking into account the

balance between reactions (2) and (3) in the second step of the proposed dissolution model. These findings provide important insights into the growth and dissolution mechanisms of calcite and other carbonate minerals constituting Earth's upper crust, under a wide range of natural conditions. Future systematic studies by high-speed FM-AFM, in combination with other experimental and simulation techniques, should ultimately enable accurate and robust prediction of long-term and large-scale carbon cycles, for example, in the GCS, weathering of buildings, and changes in the global climate and landforms.

ASSOCIATED CONTENT

Supporting Information.

The following files are available free of charge.

Supplementary Document: the explanation of the AFM experiments, classical MD simulation and DFT calculations and supplementary figures S1-S10 (PDF).

Supplementary Video 1: Successive FM-AFM images of calcite ($10\bar{1}4$) surface obtained in water. 2 s/frame. $\Delta f = 2.86$ kHz. $A = 0.13$ nm. 10×10 nm², 500×500 pix². Three images were selected and shown in Figure 2b (MPG).

Supplementary Video 2: MD simulation model showing the thermal fluctuation of the adsorbed Ca²⁺ (green) and OH⁻ (red) ions at the step edge of the calcite ($10\bar{1}4$) surface in water. The movie shows the last 0.5 ns of the total simulation time (7.5 ns) (MPG).

Supplementary Video 3: MD simulation model showing the thermal fluctuation of the adsorbed Ca^{2+} (green), OH^- (red) and HCO_3^- (blue) at the step edge of the calcite ($10\bar{1}4$) surface in water. The movie shows the last 0.5 ns of the total simulation time (7.5 ns) (MPG).

AUTHOR INFORMATION

Corresponding Author

*E-mail: adam.foster@aalto.fi (A.S.F.)

*E-mail: fukuma@staff.kanazawa-u.ac.jp (T.F.)

Present Addresses

|| Bio-AFM Frontier Research Center, Kanazawa University, Kanazawa 920-1192, Japan

Author Contributions

The AFM experiments were performed in the group of T.F. while the simulations were performed in the group of A.S.F. K. Miyata and T. F. developed the high-speed FM-AFM. K. Miyata obtained most of the AFM images in the manuscript while Y. K. obtained those in Figure S4. J. T. and P. S. performed the classical MD simulations while V. H. performed the DFT calculations. K. Miyazawa developed a software to analyze the data obtained by experiments and simulations. T. F. prepared the first draft of the manuscript but all the authors contributed to the data analyses, establishment of the dissolution model and the preparation of the final version of the manuscript.

Notes

The authors declare no competing financial interest.

ACKNOWLEDGMENT

This work was supported by KAKENHI (No. 16H02111); JST ACT-C; JSPS Bilateral Joint Research Project and Kanazawa University CHOZEN Project. J. T., V. H., P. S., and A.S.F. acknowledge the support from the Academy of Finland through its Centres of Excellence Program (Project No. 915804) and EU project PAMS (Contract No. 610446), as well as the use of the CSC, Helsinki, for computational resources.

REFERENCES

- (1) Reeder, R. J. *Carbonates: Mineralogy, and Chemistry*; Reviews in Mineralogy Volume 11; Mineralogical Society of America: Washington, DC, **1983**.
- (2) Sigman, D. M.; Boyle, E. A. *Nature* **2000**, 407, 859-869.
- (3) Sarmiento, J. L.; Gruber, N. *Ocean Biogeochemical Dynamics*, Princeton University Press: New Jersey, **2006**.
- (4) Knauss, K. G.; Johnson, J. W.; Steefel, C. I. *Chem. Geol.* **2005**, 217, 339-350.
- (5) Shiraki, R.; Rock, P. A.; Casey, W. *Aquat. Geochem.* **2000**, 6, 87-108.
- (6) Truesdale, V. W. *Aquat. Geochem.* **2015**, 21, 365-396.
- (7) Arvidson, R. S.; Ertan, I. E.; Amonette, J. E.; Luttge, A. *Geochim. Cosmochim. Ac.* **2003**, 67, 1623-1634.
- (8) Laanait, N.; Callagon, E. B. R.; Zhang, Z.; Sturchio, N. C.; Lee, S. S.; Fenter, P. *Science* **2015**, 349, 1330-1334.
- (9) McCoy, J. M.; LaFemina, J. P. *Surf. Sci.* **1997**, 373, 288-299.

- (10) Hillner, P. E.; Gratz, A. J.; Manne, S.; Hansma, P. K. *Geology* **1992**, 20, 359-362.
- (11) Stipp, S. L. S.; Eggleston, C. M.; Nielssen, B. S. *Geochim. Cosmochim. Ac.* **1994**, 58, 3023-3033.
- (12) Lasaga, A. C.; Luttge, A. *Science* **2001**, 291, 2400-2404.
- (13) Kurganskaya I.; Luttge A. *J. Phys. Chem. C* **2016**, 120, 6482-6492.
- (14) Neagle, W.; Rochester, C. H. *J. Chem. Soc. Faraday Trans.* **1990**, 86, 181-183.
- (15) Kuriyavar, S. I.; Vetrivel, R.; Hegde, S. G.; Ramaswamy, A. V.; Chakrabarty, D.; Mahapatra, S. *J. Mater. Chem.* **2000**, 10, 1835-1840.
- (16) Stipp, S. L.; Hochella, M. F., Jr. *Geochim. Cosmochim. Ac.* **1991**, 55, 1723-1736.
- (17) Kerisit, S.; Parker, S. C.; Harding, J. H. *J. Phys. Chem. B* **2003**, 107, 7676-7682.
- (18) Lardge, J. S.; Duffy, D. M.; Gillan, M. J.; Watkins, M. J. *J. Phys. Chem. C* **2010**, 114, 2664-2668.
- (19) Kodera, N.; Yamamoto, D.; Ishikawa, R.; Ando, T. *Nature* **2010**, 468, 72.
- (20) Fukuma, T.; Kobayashi, K.; Matsushige, K.; Yamada, H. *Appl. Phys. Lett.* **2005**, 87, 034101.
- (21) Fukuma, T.; Onishi, K.; Kobayashi, N.; Matsuki, A.; Asakawa, H. *Nanotechnology* **2012**, 23, 135706.

- (22) Fukuma, T.; Kimura, M.; Kobayashi, K.; Matsushige, K.; Yamada, H. *Rev. Sci. Instrum.* **2005**, 76, 053704.
- (23) Fukuma, T.; Jarvis, S. P. *Rev. Sci. Instrum.* **2006**, 77, 043701.
- (24) Fukuma, T. *Rev. Sci. Instrum.* **2009**, 80, 023707.
- (25) Mitani, Y.; Kubo, M.; Muramoto, K.; Fukuma, T. *Rev. Sci. Instrum.* **2009**, 80, 083705.
- (26) Miyata, K.; Asakawa, H.; Fukuma, T. *Appl. Phys. Lett.* **2013**, 103, 203104.
- (27) Miyata, K.; Usho, S.; Yamada, S.; Furuya, S.; Yoshida, K.; Asakawa, H.; Fukuma, T. *Rev. Sci. Instrum.* **2013**, 84, 043705.
- (28) Akrami, S. M. R.; Miyata, K.; Asakawa, H.; Fukuma, T. *Rev. Sci. Instrum.* **2014**, 85, 126106.
- (29) Hillner, P. E.; Manne, S.; Gratz, A. J.; Hansma, P. K. *Ultramicroscopy* **1992**, 42-44, 1387-1393.
- (30) Stipp, S. L. S. *Geochim. Cosmochim. Ac.* **1999**, 63, 3121-3131.
- (31) Rode, S.; Oyabu, N.; Kobayashi, K.; Yamada, H.; Kühnle, A. *Langmuir* **2009**, 25, 2850-2853.
- (32) Spagnoli, D.; Kerisit, S.; Parker, S. C. *J. Cryst. Growth* **2006**, 294, 103-110.
- (33) De La Pierre, M.; Raiteri, P.; Gale, J. D. *Crystal Growth & Design* **2016**, 16, 5907-5914.

- (34) Loerting, T.; Tautermann, C.; Kroemer, R. T.; Kohl, I.; Hallbrucker, A.; Mayer, E.; Liedl, K. R. *Angew. Chem. Int. Ed.* **2000**, 39, 891-894.
- (35) Ruiz-Agudo, E.; Kudłacz, K.; Putnis, C. V.; Putnis, A.; Rodriguez-Navarro, C. *Environ. Sci. Technol.* **2013**, 47, 11342-11349.
- (36) Amano, K.-I.; Suzuki, K.; Fukuma, T.; Takahashi, O.; Onishi, H. *J. Chem. Phys.* **2013**, 139, 224710.
- (37) Watkins, M.; Reischl, B. *J. Chem. Phys.* **2013**, 138, 154703.
- (38) Miyazawa, K.; Kobayashi, N.; Watkins, M.; Shluger, A. L.; Amano, K.-I.; Fukuma, T. *Nanoscale* **2016**, 8, 7334-7342.
- (39) Giessibl, F. *J. Appl. Phys. Lett.* **2001**, 78, 123-125.
- (40) Tracey, J.; Miyazawa, K.; Spijker, P.; Miyata, K.; Reischl, B.; Canova, F. F.; Rohl, A. L.; Fukuma, T.; Foster, A. S. *Nanotechnology* **2016**, 27, 415709.
- (41) Nada, H. *J. Phys. Chem. C* **2014**, 118, 14335-14345.
- (42) Ruiz-Agudo, E.; Kowacz, M.; Putnis, C. V.; Putnis, A. *Geochim. Cosmochim. Acta.* **2010**, 74, 1256-1267.
- (43) Demadis, K. D.; Lykoudis, P.; Raptis, R. G.; Mezei, G. *Cryst. Growth Des.* **2006**, 6, 1064-1067.

TOC Graphic

